

CFAT: Unleashing Triangular Windows for Image Super-resolution

Abhisek Ray
Indian Institute of Technology Patna
rayabhisek0610@gmail.com

Gaurav Kumar
Indian Institute of Technology Patna
gaurav19.iitp@gmail.com

Maheshkumar H. Kolekar
Indian Institute of Technology Patna
mahesh@iitp.ac.in

<https://github.com/rayabhisek123/CFAT>

Abstract

Transformer-based models have revolutionized the field of image super-resolution (SR) by harnessing their inherent ability to capture complex contextual features. The overlapping rectangular shifted window technique used in transformer architecture nowadays is a common practice in super-resolution models to improve the quality and robustness of image upscaling. However, it suffers from distortion at the boundaries and has limited unique shifting modes. To overcome these weaknesses, we propose a non-overlapping triangular window technique that synchronously works with the rectangular one to mitigate boundary-level distortion and allows the model to access more unique sifting modes. In this paper, we propose a Composite Fusion Attention Transformer (CFAT) that incorporates triangular-rectangular window-based local attention with a channel-based global attention technique in image super-resolution. As a result, CFAT enables attention mechanisms to be activated on more image pixels and captures long-range, multi-scale features to improve SR performance. The extensive experimental results and ablation study demonstrate the effectiveness of CFAT in the SR domain. Our proposed model shows a significant 0.7 dB performance improvement over other state-of-the-art SR architectures.

1. Introduction

Efficient transmission or storage of images in band- or memory-limited systems heavily relies on diverse image compression techniques. However, in the real world, these image compression phenomena are lossy. It is challenging to retrieve the original visual quality from its compressed correspondent. Image super-resolution (SR) [10], a reverse engineering approach in contrast to compression, aims to recover high-resolution (HR) images from their

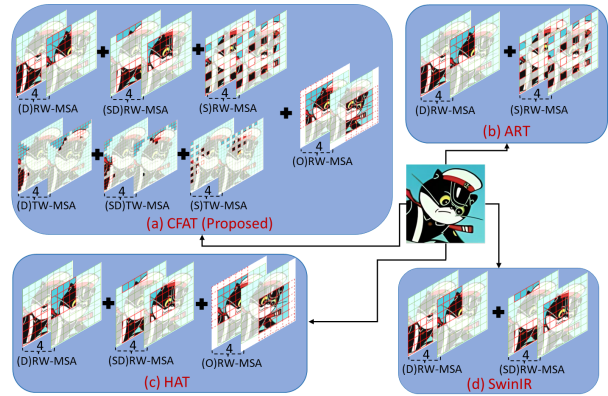


Figure 1. Proposed CFAT vs other SOTA models. RW/TW: Rectangular/Triangular Window, MSA: Multi-Head Attention, (D): Dense, (SD): Shifted Dense, (S): Sparse, (O): Overlapping

low-resolution (LR) counterparts. Despite extensive and consistent research efforts, SR models still struggle to eliminate the visual artifacts in recovered images entirely. In early 2014, the evolution of deep neural networks enhanced SR capabilities with CNN as a mainframe skeleton [10]. These approaches [9, 20, 45, 46] frequently come with substantial computational and memory requirements regardless of their effectiveness. The transformer-based techniques have stood out as the most successful SR approaches among many emerging models, showcasing state-of-the-art performances in the recent era.

The surge in popularity of transformer-based architectures is attributed to their natural proficiency in leveraging long-range dependencies among image features. Leading approaches such as SwinIR [26], Swin2SR [8], ESRT [29], HST [22], HAT [6] and ART [44] advocate the above benefit. They predominantly rely on a hierarchical attention mechanism, ensuring the reconstruction of HR outputs from their LR counterparts with enhanced precision.

SwinIR [28] pioneered the application of the shifted window technique in the domain of image restoration [26], fo-

cusing mainly on image super-resolution. Swin2SR [8] re-defined the SwinIR to enhance the performance after effectively tackling data and training-related challenges. However, both [26] and [8] consistently concentrate exclusively on specific image patches for self-attention. The dilated window approach introduced in ART [44] aims not only to resolve the fixed window problem as mentioned earlier but also to alleviate computational load while concurrently boosting super-resolution performance. Nevertheless, the quick internal switching between dense and sparse attention layers, each tailored to specific receptive fields, imposes constraints on overall performance. HAT [5] outperforms other prominent super-resolution architectures by a significant 1 dB margin, achieved through integrating global channel attention with local window-based self-attention. The incorporation of the overlapping shifted window technique effectively addresses concerns related to repetitive image patches, while the introduction of channel attention substantially enhances super-resolution performance. Drawing inspiration from the CNN-transformer model, ACT [41] strategically positions both CNN and transformer within two distinct streams to concurrently leverage global and local features. The harmonious, complementary features on both branches interchange relatable information with one another through a channel split fusion block based on cross-scale token attention (CSTA). The above-discussed state-of-the-art transformer-based methods use a rectangular shifted window-based self-attention mechanism. The repetitive use of rectangular window attention at each layer is susceptible to causing boundary-level distortion, as the participation of neighbors for boundary pixels is limited. In addition to this, the symmetrical structure of the rectangular window restricts the range of unique shifting modes available for covering the entire image patches. The presence of boundary-level distortion and a limited range of shifting modes in the shifted rectangular window technique could potentially hinder its effectiveness, extending beyond super-resolution to other computer vision tasks.

To tackle the challenges mentioned earlier, we propose a pioneering triangular window technique. This novel window technique helps boost the performance for super-resolution tasks and all computer vision applications where the rectangular window technique is predominantly used. This paper seamlessly incorporates the proposed triangular window with the conventional rectangular window in a transformer framework called Composite Fusion Attention Transformer (CFAT). Integrating a channel-based global attention unit with the above triangular-rectangular window-based local self-attention further improves the performance of single-image SR. The above attention pair belongs to the non-overlapping attention category and effectively leverages local and global image features. To exploit the overlapping image features, we place an overlapping cross-fusion

attention block (OCFAB) at the end of each unit block called the Dense Window Attention Block (DWAB). The proposed model, CFAT, offers several unique advantages: (i) The combined window-based self-attention technique eliminates the boundary level distortion issue that arises during traditional rectangular window-based self-attention. (ii) Embracing a triangular window offers a broader range of shifting modes, thereby expanding spatial features and enhancing overall performance. (iii) OCFAB leverages overlapping spatial image features, resulting in a further enhancement of performance.

The proposed CFAT network delivers superior SR results across multiple benchmark datasets, notably outperforming recent transformer-based SR techniques [22, 28]. The novelty of our paper in comparison to other state-of-the-art methods like SwinIR [28], ART [44], and HAT [5] is outlined in Fig. 1. Our contributions in this paper can be summarized as:

1. We are the first to introduce the triangular windowing mechanism in the computer vision task. We smoothly integrate it with traditional rectangular windows to employ non-overlapping self-attention in single-image SR. This combination phases out the constraints associated with the conventional rectangular window approaches like boundary-level distortion and restricted unique shifting modes.
2. This window mechanism is beneficial not only in super-resolution tasks but also in various other computer vision applications that implement the rectangular window technique in their mainframe.
3. We propose a CFAT that exploits local and global image features through overlapping and non-overlapping spatial and channel attention, respectively.
4. Through comprehensive evaluations on multiple benchmark SR datasets, our method has delivered superior performance compared to other state-of-the-art methods.

2. Related Works

2.1. CNN Based Super-Resolution

Initially, most single-image super-resolution (SISR) approaches relied heavily on convolutional neural networks (CNNs) due to their remarkable spatial feature extraction capability over traditional machine learning approaches. SRCNN [11] stands as a pioneering effort, leveraging a shallow three-layer CNN architecture to map low-resolution (LR) images to their high-resolution (HR) counterparts. However, a sharp decline in performance is observed while increasing the number of CNN layers intended for extracting more complex features. EDSR [27] is an SR architecture based on the Residual Network (ResNet) framework, which mitigates this limitation by including shortcut connections. Introducing channel attention mechanisms

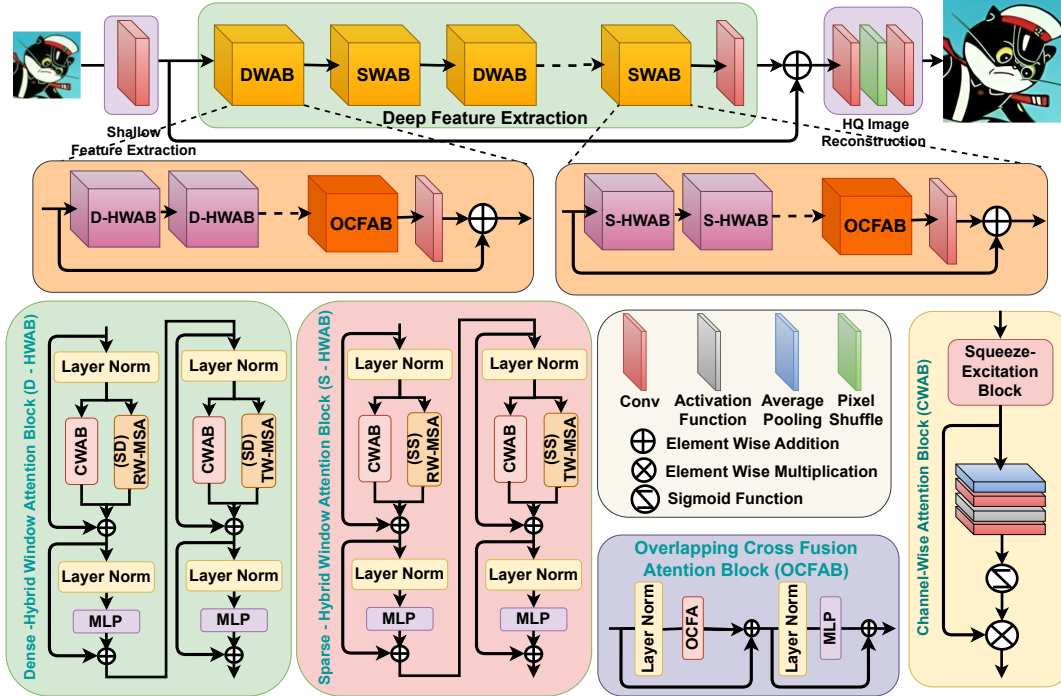


Figure 2. The overall architecture of CFAT with all internal units.

in super-resolution, RCAN [45] presents a unique residual-in-residual (RIR) design. RDN [46] utilizes a residual dense block (RDB) that efficiently extracts ample local features through densely interconnected CNN layers. SAN [9] is built upon a second-order attention network that takes SR performance to a new height. LatticeNet [30] incorporates the Fast Fourier Transform (FFT) technique to construct a lattice design, enabling lightweight super-resolution. [12, 15, 19, 21, 27, 35], and [18] are other prominent CNN-based SR models that demonstrate notable advancement in performances over their predecessors. These models incorporate advanced CNN architectures, such as residual blocks [27, 45], dense blocks [46], and attention mechanisms [15, 35], to enhance feature generalization, ultimately leading to superior outcomes. While CNN-based methods have seen significant success in SISR, they do come with limitations. Specifically, they can only extract local features from images, and they often entail high computational costs for both training and deployment.

2.2. Vision Transformer (ViT) Based SR

The transformer architecture [38] operates on the principle of self-attention, a technique that generalizes features in terms of a global spatial perspective and can capture long-range dependencies between them. ViT, introduced in [13], is evident as the first work to substitute standard convolution with the transformers in high-level vision tasks. Following this, in many computer vision applications, including image recognition [25, 34], object detection [3, 7], image segmentation [2, 16], and image SR [31, 36, 42, 47], transformer-based architecture replaces conventional CNN-based mod-

els to elevate their performances. Building on transformer models, SwinIR [26] employs the Swin transformer with window-based self-attention for image restoration. Its improved version, Swin2SR [8], utilizes the SwinV2 transformer specifically for compressed image super-resolution and restoration tasks. Meanwhile, ESRT [29] introduces efficient transformers that achieve competitive results at a reduced computational cost. ART [44] incorporates both sparse and dense attention modules within a single network that aim to refine image restoration results. In a recent advancement, [6] introduced a transformer architecture, HAT, which combines channel attention with overlapping and non-overlapping self-attention mechanisms to activate more pixels, thereby generalizing both global and local spatial features. Although the Vision Transformer has shown its superiority in modeling long-range dependencies, there are still many works that demonstrate that the convolution can help the transformer to achieve better visual representation [23, 39, 40]. Drawing inspiration from the CNN-transformer model, ACT [41] strategically places both CNN and transformer within two distinct streams to concurrently leverage global and local features. The above SR models adopt a shifted rectangular window technique to limit their spatial features for effective localized self-attention. In contrast, these models experience boundary-level distortion and encounter limitations in shifting modes when exclusively relying on the rectangular window technique. In this paper, we propose a pioneering triangular window technique that works alongside a rectangular one to wipe out these drawbacks in SISR.

3. Proposed Method

3.1. Overall Architecture

As presented in Fig.2, the entire network can be split into three segments: the head, body, and tail. The head module is responsible for shallow feature extraction, the body extracts the deep features, and the tail module reconstructs the HR images from LR counterparts at the output stage. The in-depth depiction of the above three is as follows:

3.2. Head Module - Shallow Feature Extractor:

We feed the input image, $I_{LR} \in \mathbb{R}^{H \times W \times C_{in}}$ to a feature extractor to get shallow output $F_{sh} \in \mathbb{R}^{H \times W \times C}$, where H , W , C_{in} , and C are the height, width, input channel count and output channel count of the respective image. This extractor is a single convolution layer of kernel size 3×3 .

$$F_{sh} = f_H(I_{LR}) \quad (1)$$

3.3. Body Module - Deep Feature Extractor:

The alternative units of Dense Window Attention Blocks (DWAB) and Sparse Window Attention Blocks (SWAB) are ultimately combined with a convolution layer to form the deep extractor module. The shallow output from the head module, $F_{sh} \in \mathbb{R}^{H \times W \times C}$, is passed through this deep extractor to yield deep features $F_{dp} \in \mathbb{R}^{H \times W \times C}$. Each unit of DWAB and SWAB is comprised of both rectangular and our proposed triangular window attention units in dense and sparse configurations, respectively.

3.3.1 Dense Window Attention Blocks (DWAB)

Each unit of DWAB implements both non-overlapping and overlapping dense window attention that helps to integrate deep and diverse features into a single network. Our design incorporates multiple units of non-overlapping attention units, called Dense-Hybrid Window Attention Block (D-HWAB), initially to get deep features and place an overlapping attention unit, called Overlapping Cross Fusion Attention Block (OCFAB), at the end to get diverse features as well. A 3×3 convolution layer at the end makes the features richer and more effective, as cited in [23, 39, 40]. Mathematically, the DWAB can be represented as

$$F_{dp} = f_{conv}(f_{op}(f_{nop}^n \dots (f_{nop}^2(f_{nop}^1(F_{sh})))))) + F_{sh}, \quad (2)$$

where, f_{nop}^x , f_{op} , and f_{conv} stands for non-overlapping, overlapping and convolution operations, respectively.

Dense-Hybrid Window Attention Block (D-HWAB):

The underlying module advocates dense attention, alternatively combining shifted rectangular and novel triangular transformer units. The Multi-head Self Attention (MSA) carried out in both units is called Shifted-Dense Rectangular Window MSA ((SD)RW-MSA) and Shifted-Dense Triangular Window MSA ((SD)TW-MSA). Both of them execute non-overlapping self-attention. The combination of channel attention features from Channel Wise Attention Block (CWAB) and spatial attention features from (SD)RW-MSA

and (SD)TW-MSA in both transformer units, as shown in Fig.2, elevates the overall performance. The overall computation can be represented as

$$F_{DA} = f_{nop}^x(F_{sh}) = f_{tri}^n f_{rect}^n \dots (f_{tri}^1(f_{rect}^1(F_{sh}))), \quad (3)$$

where, F_{DA} , f_{rect}^x , and f_{tri}^x are dense attention features, rectangular and triangular window dense attention, respectively. The output feature from rectangular transformer unit can be expressed as

$$F_{int} = f_{MSA}^{rect}(f_{LN}^1(F_{in})) + \alpha f_{CA}(f_{LN}^1(F_{in})) + F_{in}, \quad (4)$$

$$F_{out} = f_{MLP}(f_{LN}^2(F_{int})) + F_{int}, \quad (5)$$

where, F_{in} , F_{int} , and F_{out} are input, intermediate and output features respectively. f_{MSA}^{rect} , f_{LN}^1 , f_{LN}^2 , and f_{CA} are the feature transformation in (SD)RW-MSA, first Layer-Norm, second LayerNorm and CWAB respectively. Similarly, the output feature from triangular transformer unit can be expressed as

$$F_{int} = f_{MSA}^{tri}(f_{LN}^1(F_{in})) + \beta f_{CA}(f_{LN}^1(F_{in})) + F_{in}, \quad (6)$$

$$F_{out} = f_{MLP}(f_{LN}^2(F_{int})) + F_{int}, \quad (7)$$

where, f_{MSA}^{tri} is the feature transformation of (SD)TW-MSA. The α in equation 4 and β in equation 6 are two hyper-parameter to limit the dominance of channel attention in F_{out} of rectangular and triangular transformer units respectively.

Overlapping Cross Fusion Attention Block (OCFAB):

This block overlaps the features across neighboring windows and establishes cross-attention between them to improve performance further. The underlying attention is called Overlapping Cross Fusion Attention (OCFA). The OCFAB is implemented by a sliding window approach called unfolding operation, using a kernel of size R_0 , a stride of R , and padding of $\frac{kR}{2}$ zeros to make the sizes compatible for overlapping. The input feature of dimension $H \times W \times C$ are divided into $\frac{HW}{R^2}$ overlapping windows of size R_0 . Here, R_0 is determined by

$$R_0 = (1 + k)R, \quad (8)$$

where 'k' is a constant regulating overlapping ratio and R represents the size of window before overlapping. During MSA, the query is calculated by a linear layer, whereas key and value are produced by a linear layer followed by an unfolding operation. The OCFAB block is present at the end of both DWAB and SWAB, as shown in Fig. 2.

Channe-Wise Attention Block (CWAB): Most studies show the practice of using standard convolution while executing squeeze-excitation channel attention [6]. However, we use depthwise-pointwise convolution that helps to reduce the squeeze factor without increasing the computational burden. Therefore, we design CWAB with a GELU activation function sandwiched between two depthwise-pointwise convolutional layers followed by a channel-wise attention module at the end.

3.3.2 Sparse Window Attention Block (SWAB)

Like DWAB, SWAB promotes non-overlapping and overlapping window attention on sparse windows instead of dense ones. This block also includes four operations as shown in Fig.2: (i) non-overlapping rectangular sparse window attention, (ii) non-overlapping triangular sparse window attention, (iii) overlapping cross-fusion attention, and (iv) convolution operation. The latter two are the same as discussed in Sec. 3.3.1, but the former two are a little different in terms of rectangular and triangular window formation compared to DWAB. First, we prepare sparse windows from the input of dimension $H \times W \times C$ by maintaining a regular gap, called interval size I , between consecutive input features. After that, we follow the standard rectangular and triangular window techniques to implement respective attention. Sec. 4 provides more details about triangular sparse attention. We follow a similar procedure in implementing rectangular sparse attention.

3.3.3 Tail Module - HQ Image Reconstruction

In the final stage, we obtain the upscaled input signal (I_{SR}) by passing the deep features (F_{dp}) from body through a pixel-shuffle layer sandwiched between a pair of convolution layers. This is represented by $I_{SR} = f_T(F_{dp})$.

4. Triangular Window Technique

Design: Considering an input image I_{in} of dimension $H \times W \times C$, we first divide this input into $\frac{HW}{M^2}$ rectangular windows of size $M \times M$. Then, each rectangular patch is again split into four triangular windows as displayed in Fig.3. In this figure, we take M as 32, which provides four triangular masks of linear dimension 16×16 . These four triangular windows are called upper, right, lower, and left triangular windows. The corresponding rectangular windows are also shown in this figure.

Advantages over Rectangular Window: In computer vision, the attributes of a pixel depend on itself and its neighbor as well. As a result, the edge pixels of the rectangular window are not as effectively explored as the interior pixels during self-attention, leading to distortions at the boundaries. The distortion will become so pronounced that it will ultimately deteriorate model performance. The above problem can be prominently seen in both rectangular and triangular windows while implemented alone. Therefore, we combine the rectangular window-based MSA with our proposed triangular one in series. This alternative configuration of rectangular and triangular transformers mitigates the edge-level distortion of one another.

Many studies confirm that the shifted rectangular window, in conjunction with the non-shifted version, can vastly enhance the SR performance [6, 8, 26, 44]. However, we can observe a restriction in shifting the rectangular window as repetition occurs due to its isometric geometry. From

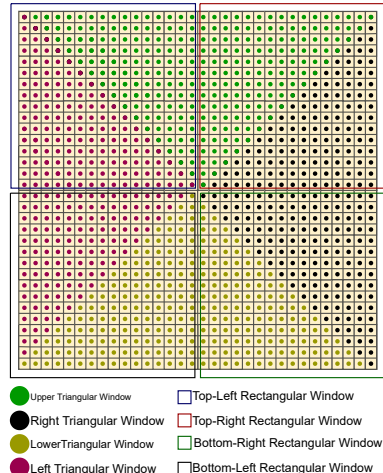


Figure 3. A rectangular and triangular patch in 32×32 window.

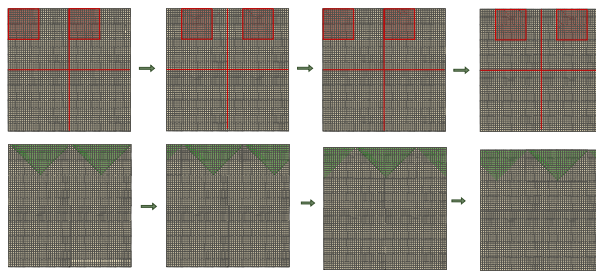


Figure 4. Shifting modes of rectangular and triangular windows in a 64×64 image patch

Fig.3, it is noticeable that the coverage length of the triangular window is more than the rectangular one in x-dimension. Due to this extended coverage, the triangular windows are allowed more non-identical shifts than rectangular windows. As shown in Fig.4, the rectangular window has non-identical shifting modes of 0 and 8, whereas the triangular window has 0, 8, 16, and 24. The availability of more unique shifting modes in triangular windows enhances the model’s performance further than rectangular ones by mitigating the edge-related artifacts at the boundaries, aligning the features that contribute to improving localization accuracy and providing greater adaptability to noncentralized image patterns.

Due to the structural heterogeneity that exists between rectangular and triangular window patches, as shown in Fig. 3, the spatial features that participated in the alternative connection of triangular and rectangular self-attention inside DWAB or SWAB are different from each other. These diverse activated features from successive triangular and rectangular attention leverage more diverse spatial features to participate in HR reconstruction. It boosts the performance further.

Computational Cost: The first step of MSA used in transformer calculates query $q = xw_q$, key $k = xw_k$ and value $v = xw_v$ matrices for an input $x \in R^{HW \times C}$

and the corresponding three trainable parameter matrices $w_q \in R^{C \times C_a}$, $w_k \in R^{C \times C_k}$, and $w_v \in R^{C \times C_v}$. In our case, we consider $C=C_q=C_k=C_v$ and $HW \gg C$. For mathematical convenience, we assume the number of heads equals 1. Considering space complexity for (i) qk^T/\sqrt{C} equal to $O([HW]^2C)$, (ii) exponential and row sum operations of softmax equal to $O([HW]^2)$, (iii) division operation of softmax equal to $O([HW]^2)$, and value multiplication operation equal to $O([HW]^2C)$, the approximate computational complexity of MSA is

$$O(MSA) = 4[HW]C^2 + 2[HW]^2C \quad (9)$$

The above equation confirms the high computational cost of deploying ViTs. The rectangular window technique is the only solution to lower the complexity so far. However, we proposed a triangular window technique that not only reduces the computational burden but also yields better results than a rectangular counterpart while working alone and even produces superior performance while employed synchronously with a rectangular window. In this paper, we introduce two variants of attention relating to the proposed triangular window: (i) dense triangular attention and (ii) sparse triangular attention.

The dense triangular attention has a 1D token size of L^2 , where L is the triangular window equivalent of rectangular window token $L \times L$. The computational cost of the proposed dense TW-MSA is

$$O(D-MSA) = (4HWC^2 + 2HWL^2C) \quad (10)$$

The effective sequence length in sparse triangular attention is the same as dense but for a wider receptive field. The interval length S controls the sparsity in the triangular window during the attention mechanism. S can be compared with the stride in convolution operation. The computational cost of sparse TW-MSA in terms of parameter S is

$$O(S-MSA) = (4HWC^2 + 2(\frac{HW}{S})^2C) \quad (11)$$

The computational cost of dense TW-MSA and sparse TW-MSA are drastically improved as $L^2 \ll HW$ in equation 10 and $(\frac{HW}{S})^2 \ll (HW)^2$ in equation 11, respectively.

5. Experiments

5.1. Datasets and Performance Matrices

We train the proposed model with two widely used DIV2K [37] and Flickr2K [27] datasets to avoid overfitting while training only on DIV2K and evaluate on standard SR benchmarks: Set5 [1], Set14 [43], BSD100 [32], Urban100 [17], and Mangal09 [33]. We evaluate the proposed SR model using PSNR and SSIM on the Y channel in YCbCr Space.

5.2. Experimental Settings

We perform geometric data augmentation where each training sample is replaced by its flipped or rotated (90°, 180°, and 270°) equivalent. The augmented input samples are then cropped into 64×64 patches before passing

through the model. While configuring the proposed CFAT, we put 3 DWAB and 3 SWAB in an alternative order. We maintain 4 D-HWAB and 4 S-HWAB inside each DWAB and SWAB unit, respectively. Here, each D-HWAB and S-HWAB unit represents a unique shift size, i.e., 0, 8, 16, and 24. We take 180 channels, while attention heads and window sizes are set to 6 and 16 for all units of (SD)RW-MSA, (S)TW-MSA, and OCFA. Other hyperparameter values are discussed in the ablation study. We set the batch size to 32. We use ADAM optimizer for model training with $\beta_1 = 0.9$ and $\beta_2 = 0.999$. The weight decay is set to zero. The total iteration during training is set to 250K. The initial learning rate is set to 2e-4, which is reduced to half after [112.5K, 175K, 200K, 225K] iterations. We use L_1 loss for model training. We take the pre-trained ×2 model and finetune it for ×4 resolution. We also introduced a more compact CFAT, namely CFAT-S, with 144 channels, featuring a depthwise-pointwise convolution in CWAB. The experiments are performed using Python 3.10.11 based PyTorch 2.0.1 deep learning framework on an Ubuntu 20.04.2 machine with A100-PCIE-40GB GPU enabled with Nvidia CUDA 10.1.243 and CuDNN 8.1.0.

Table 1. Performance based on various triangular & rectangular window size, and shift size. L: Linear, S: Square.

Triangular window size	8*8 (L)	16*16 (L)			
PSNR (in dB)	27.58	27.77			
Rectangular window Size	8 (S)	12 (S)	16 (S)		
PSNR (in dB)	27.52	27.64	27.77		
Shift Size	0	8	16	24	all
PSNR (in dB)	27.58	27.68	27.67	27.66	27.77

Table 2. Ablation study for α , β , and channel counts.

α	0	1	0.1	0.01
PSNR (in dB)	27.70	27.67	27.61	27.77
β	0	1	0.1	0.015
PSNR (in dB)	27.72	27.65	27.69	27.78
Channel Count	180	144	96	
PSNR (in dB)	27.77	27.45	27.21	

Table 3. Performance based on overlapping constant.

I	0	2	4	6
PSNR(dB)	27.75	27.76	28.72	27.70
k	0	0.25	0.5	0.75
PSNR(dB)	27.68	27.65	27.77	27.72

Table 4. Ablation study for CWAB, RWAB, and TWAB.

Structure	w/o CWAB	w/ CWAB	CWAB with DP conv
PSNR/SSIM	27.65dB/0.7481	27.75dB/0.7489	27.77dB/0.7494
Structure	w/o RWAB	w/o TWAB	w/ RWAB & TWAB
PSNR/SSIM	27.61dB/0.7463	27.56dB/0.7471	27.77dB/0.7494

5.3. Ablation Study

5.3.1 Impact of Various Model Hyperparameters :

To realize the impact of various model hyperparameters, we conduct all our experiments on BSD100 dataset for a scale of $\times 4$ and a epoch of 70 and compute the model’s performance in terms of PSNR.

Window Size and Shift Size : In [6], the authors reveal that optimum rectangular window size can activate more pixels that in turn elevate model performances. [24] and [6] investigate their model with square patch sizes of (8, 12) and (8, 16) respectively. In this paper, we inspect our model on the square patch of (8, 12, 16) for the rectangular and linear patch of (8*8, 16*16) for triangular windows. The experimental results are shown in Tab. 1. Again, we evaluate the performance with (8, 16, 24, variable) shift and without shift (0), which is also mentioned in this table. Here, the ‘variable’ refers to varying shift size from $0 \rightarrow 8 \rightarrow 16 \rightarrow 24$ in succession. From the above, we can conclude that the model yields the best PSNR for 16*16 triangular linear-window, 16×16 rectangular square-window, and variable shift size.

Interval Size : Interval size (I) plays a decisive role in estimating model performance [44]. A smaller I refers to the wide receptive field with high computation, and a larger I implies the opposite. However, we prioritize the performance and compute model results by varying the I . We can observe from Tab. 3 that the model gives the best performances for interval sizes 0 and 2. However, we chose $I = 2$ as it allows us to design our model with fewer computations.

α, β , Channel Counts and CWAB: To examine the influence of weighing factor α and β , we measure the model outcome for four different values (0, 1, 0.1, 0.01) of α and β separately. As displayed in Tab. 2, these experiments specify the optimum value of α and β as 0.01 and 0.015, respectively. We also scrutinize the effect of channel count in CFAT as shown in Tab. 2. We select 180 as the channel counts for CFAT as the rise in channel non-linearly increases the model parameters, and also, the model performance slowly gets saturated after 180.

Overlapping Constant : In OCFAB, we use a constant k to determine the overlapping range between two consecutive windows during cross-attention. We study the impact of various overlapping ratios by adjusting k values ranging from 0 to 0.75, and the results are presented in Tab. 3. Here, $k = 0$ corresponds to a standard Transformer block. The results displayed in this table indicate that the model delivers optimal performance for $k = 0.5$.

5.3.2 Impact of CWAB :

We have performed three experiments to study the importance of CWAB. From Tab. 4, it is quite evident that the PSNR value of CFAT without CWAB is 0.1dB lower than CFAT using CWAB with standard convolution. However,

we get a slight performance advantage when it comes to model outcomes with CWAB using depthwise-pointwise (DP) convolutions and lower squeeze factor. So, we get a better result without a computational trade-off, as the latter two have the same complexity.

5.3.3 Impact of Triangular and Rectangular Windows:

In CFAT, RWAB and TWAB modules carry significant roles in CFAT realization. From Tab. 4, we can observe a significant drop of $0.21 \sim 0.16$ in PSNR for our model without TWAB or RWAB. These results confirm our design of including both units in the final model. They combinely truncate the effect of edge-level distortion that leads to enhanced performance. In this table, we also observe a narrow advantage for TWAB over RWAB when individually evaluated due to the feasibility of extra shifting modes.

5.4. Comparisons with State-of-the-art Methods

Quantitative Analysis : We select CNN-based EDSR [27], SAN [9], and HAN [35] with transformer-based IPT [4], SwinIR [26], Swin2SR [8], ACT [41], ART [44], EDT [24], HAT [6] state-of-the-art architectures to compare our model quantitatively in term of PSNR and SSIM. Tab. 5 presents the quantitative comparison of CFAT based on scale factors $\times 2$, $\times 3$, and $\times 4$ for both DIV2K and DF2K (DIV2K+Flickr2K) training datasets. HAT [6] is considered the previous best model whose outcome outplays any other SOTA models. However, due to the undistort and rich feature exploration capability of CFAT, it yields superior performances than HAT [6] for all scale factors across all five benchmark datasets. The superior results confirm the significance of using triangular window attention in CFAT. The small variant of CFAT, called CFAT-s, is also very competitive while comparing its outcomes with some well-known transformer-based architectures like IPT [4], SwinIR [26] and Swin2SR [8].

Visual Analysis : For visual assessment, we select an image from each of the four distinct testing datasets: “img_003” from Set5, “img_072” from Urban100, “img_013” from Set14, and “img_005” from BSD100. CFAT retrieves all these images with less blur and fair lattice content, as shown in Fig.5. The PSNR and SSIM value for each image in this figure confirms our model’s superiority over all SOTA models. Our model reduces the pixel level distortion more efficiently than any other CNN- and transformer-based leading models due to the inclusion of dense and sparse triangular window attention.

Comparison based on Computational Cost : From Tab. 6, we observe that the performance of CFAT outperforms other SOTA models with a balanced trade-off between parameter and multi-add count. Our model has a few more parameters than HAT [6] but shows fewer counts of multi-adds while giving superior results on the BSD100 dataset.

Table 5. Quantitative comparison of the CFAT with various state-of-the-art SR methods.
red and green color indicate the best and second best respectively

Method	Scale	Training Dataset	Set5		Set14		BSD100		Urban100		Manga109	
			PSNR	SSIM	PSNR	SSIM	PSNR	SSIM	PSNR	SSIM	PSNR	SSIM
EDSR [27]	×2	DIV2K	38.11	0.9602	33.92	0.9195	32.32	0.9013	32.93	0.9351	39.10	0.9773
HAN [35]	×2	DIV2K	38.27	0.9614	34.16	0.9217	32.41	0.9027	33.35	0.9385	39.46	0.9785
SAN [9]	×2	DIV2K	38.31	0.9620	34.07	0.9213	32.42	0.9028	33.10	0.9370	39.32	0.9792
IPT [4]	×2	ImageNet	38.37	-	34.43	-	32.48	-	33.76	-	-	-
SwinIR [26]	×2	DIV2K+Flickr2K	38.46	0.9624	34.61	0.9260	32.55	0.9043	33.95	0.9433	40.02	0.9800
Swin2SR [8]	×2	DIV2K+Flickr2K	38.43	0.9623	34.48	0.9256	32.54	0.905	33.89	0.9431	39.88	0.9798
ACT [41]	×2	DIV2K+Flickr2K	38.53	0.9629	34.68	0.9260	32.60	0.9052	34.25	0.9453	40.11	0.9807
ART [44]	×2	DIV2K+Flickr2K	38.56	0.9629	34.59	0.9267	32.58	0.9048	34.30	0.9452	40.24	0.9808
EDT [24]	×2	DIV2K+Flickr2K	38.63	0.9632	34.80	0.9273	32.62	0.9052	34.27	0.9456	40.37	0.9811
HAT [5]	×2	DIV2K+Flickr2K	38.63	0.9630	34.86	0.9274	32.62	0.9053	34.45	0.9466	40.26	0.9809
CFAT-s (ours)	×2	DIV2K+Flickr2K	38.59	0.9621	34.81	0.92872	32.58	0.9044	34.42	0.9453	40.24	0.9799
CFAT (ours)	×2	DIV2K+Flickr2K	39.09	0.9653	35.25	0.9296	32.93	0.9072	35.01	0.9498	41.00	0.9838
EDSR [27]	×3	DIV2K	34.65	0.9280	30.52	0.8462	29.25	0.8093	28.80	0.8653	34.17	0.9476
HAN [35]	×3	DIV2K	34.75	0.9299	30.67	0.8483	29.32	0.8110	29.10	0.8705	34.48	0.9500
SAN [9]	×3	DIV2K	34.75	0.9300	30.59	0.8476	29.33	0.8112	28.93	0.8671	34.30	0.9494
IPT [4]	×3	ImageNet	34.81	-	30.85	-	29.38	-	29.49	-	-	-
SwinIR [26]	×3	DIV2K+Flickr2K	35.04	0.9322	31.00	0.8542	29.49	0.8150	29.90	0.8841	35.28	0.9543
ACT [41]	×3	DIV2K+Flickr2K	35.09	0.9325	31.17	0.8549	29.55	0.8171	30.26	0.8876	35.47	0.9548
ART [44]	×3	DIV2K+Flickr2K	35.07	0.9325	31.02	0.8541	29.51	0.8159	30.10	0.8871	35.39	0.9548
EDT [24]	×3	DIV2K+Flickr2K	35.13	0.9328	31.09	0.8553	29.53	0.8165	30.07	0.8863	35.47	0.9550
HAT [5]	×3	DIV2K+Flickr2K	35.07	0.9329	31.08	0.8555	29.54	0.8167	30.23	0.8896	35.53	0.9552
CFAT-s (ours)	×3	DIV2K+Flickr2K	34.03	0.9323	31.06	0.8551	29.57	0.8158	30.18	0.8889	35.48	0.9547
CFAT (ours)	×3	DIV2K+Flickr2K	35.31	0.9340	31.32	0.8569	29.70	0.8180	30.43	0.8928	35.82	0.9574
EDSR [27]	×4	DIV2K	32.46	0.8968	28.80	0.7876	27.71	0.7420	26.64	0.8033	31.02	0.9148
HAN [35]	×4	DIV2K	32.64	0.9002	28.90	0.7890	27.80	0.7442	26.85	0.8094	31.42	0.9177
SAN [9]	×4	DIV2K	32.64	0.9003	28.92	0.7888	27.78	0.7436	26.79	0.8068	31.18	0.9169
IPT [4]	×4	ImageNet	32.64	-	29.01	-	27.82	-	27.26	-	-	-
SwinIR [26]	×4	DIV2K+Flickr2K	32.93	0.9043	29.15	0.7958	27.95	0.7494	27.56	0.8273	32.22	0.9273
Swin2SR [8]	×4	DIV2K+Flickr2K	32.92	0.9039	29.06	0.7946	27.92	0.7505	27.51	0.8271	31.03	0.9256
ACT [41]	×4	DIV2K+Flickr2K	33.04	0.9041	29.27	0.7968	28.00	0.7516	27.92	0.8332	32.44	0.9282
ART [44]	×4	DIV2K+Flickr2K	33.04	0.9051	29.16	0.7958	27.97	0.7510	27.77	0.8321	32.31	0.9283
EDT [24]	×4	DIV2K+Flickr2K	33.06	0.9055	29.23	0.7971	27.99	0.7510	27.75	0.8317	32.39	0.9283
HAT [5]	×4	DIV2K+Flickr2K	33.04	0.9056	29.23	0.7973	28.00	0.7517	27.97	0.8368	32.48	0.9292
CFAT-s (ours)	×4	DIV2K+Flickr2K	32.01	0.9045	29.25	0.7972	27.99	0.7504	27.86	0.8358	32.45	0.9279
CFAT (ours)	×4	DIV2K+Flickr2K	33.19	0.9068	29.30	0.7985	28.17	0.7524	28.11	0.8380	32.63	0.9305

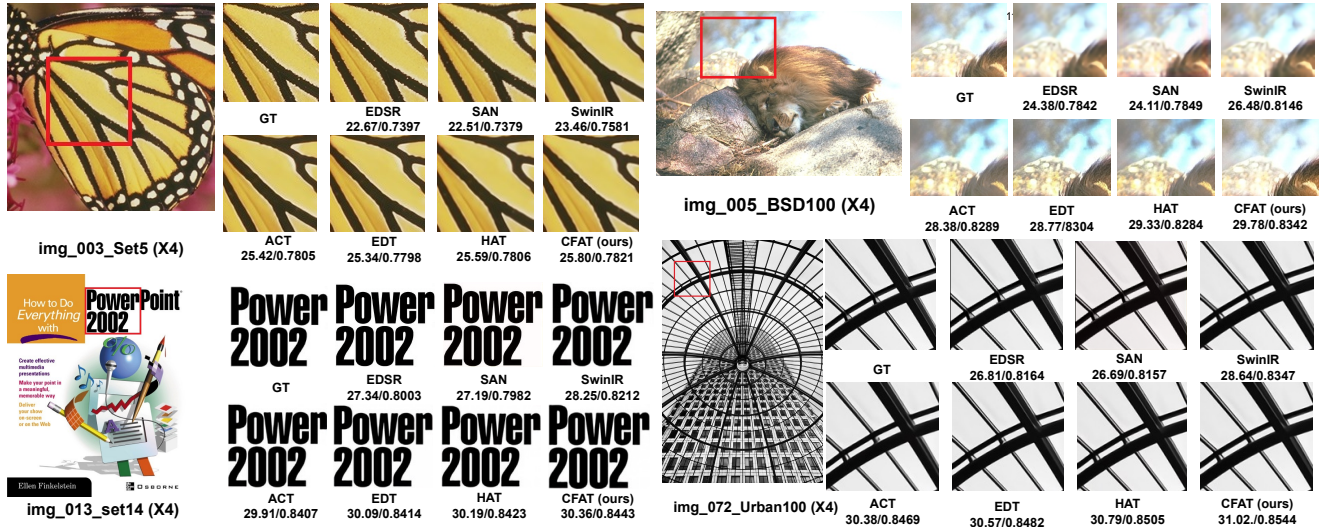


Figure 5. Visual Comparison of CFAT with other state-of-the-art methods.

Table 6. Model comparison based on computational cost

Methods	Params (M)	Multi-adds(GMac)	PSNR/SSIM
SwinIR	11.9	53.6	27.92dB/0.7489
ACT	46	22	28.00dB/0.7516
ART	16.55	120	27.97dB/0.7510
EDT	11.6	-	27.91dB/0.7483
HAT	20.8	103.7	28.00dB/0.7517
CFAT	22.07	90.59	28.17dB/0.7524

6. Conclusion

We propose a rectangular and triangular window attention-based SR architecture called Composite Fusion Attention Transformer (CFAT). This combinational design eliminates boundary-level distortion problems and

opens the gate for integrating more non-identical shifting modes. Dense and sparse attention in both windows allows interaction between local and global image features on the same platform. We also combine more diverse features through non-overlapping triangular and rectangular window-based self-attention and overlapping window-based cross-attention. Extensive experiments on multiple datasets show the effectiveness of CFAT. By incorporating the novel triangular window attention in dense, sparse, and shifted configuration, CFAT outperforms the other state-of-the-art models qualitatively and quantitatively.

References

- [1] Marco Bevilacqua, Aline Roumy, Christine Guillemot, and Marie Line Alberi-Morel. Low-complexity single-image super-resolution based on nonnegative neighbor embedding. 2012. [6](#)
- [2] Hu Cao, Yueyue Wang, Joy Chen, Dongsheng Jiang, Xiaopeng Zhang, Qi Tian, and Manning Wang. Swin-UNET: Unet-like pure transformer for medical image segmentation. In *European conference on computer vision (ECCV)*, pages 205–218. Springer, 2022. [3](#)
- [3] Nicolas Carion, Francisco Massa, Gabriel Synnaeve, Nicolas Usunier, Alexander Kirillov, and Sergey Zagoruyko. End-to-end object detection with transformers. In *European conference on computer vision (ECCV)*, pages 213–229. Springer, 2020. [3](#)
- [4] Hanting Chen, Yunhe Wang, Tianyu Guo, Chang Xu, Yiping Deng, Zhenhua Liu, Siwei Ma, Chunjing Xu, Chao Xu, and Wen Gao. Pre-trained image processing transformer. In *Computer Vision and Pattern Recognition (CVPR)*, pages 12299–12310. IEEE/CVF, 2021. [7](#), [8](#)
- [5] Xiangyu Chen, Xintao Wang, Jiantao Zhou, and Chao Dong. Activating more pixels in image super-resolution transformer. *arXiv preprint arXiv:2205.04437*, 1, 2022. [2](#), [8](#)
- [6] Xiangyu Chen, Xintao Wang, Jiantao Zhou, Yu Qiao, and Chao Dong. Activating more pixels in image super-resolution transformer. In *Computer Vision and Pattern Recognition (CVPR)*, pages 22367–22377. IEEE/CVF, 2023. [1](#), [3](#), [4](#), [5](#), [7](#), [11](#), [13](#)
- [7] Xiangxiang Chu, Zhi Tian, Yuqing Wang, Bo Zhang, Haibing Ren, Xiaolin Wei, Huaxia Xia, and Chunhua Shen. Twins: Revisiting the design of spatial attention in vision transformers. *Advances in Neural Information Processing Systems (NeurIPS)*, 34:9355–9366, 2021. [3](#)
- [8] Marcos V Conde, Ui-Jin Choi, Maxime Burchi, and Radu Timofte. Swin2sr: Swin2 transformer for compressed image super-resolution and restoration. In *European conference on computer vision (ECCV)*, pages 669–687. Springer, 2022. [1](#), [2](#), [3](#), [5](#), [7](#), [8](#)
- [9] Tao Dai, Jianrui Cai, Yongbing Zhang, Shu-Tao Xia, and Lei Zhang. Second-order attention network for single image super-resolution. In *Computer Vision and Pattern Recognition (CVPR)*, pages 11065–11074. IEEE/CVF, 2019. [1](#), [3](#), [7](#), [8](#)
- [10] Chao Dong, Chen Change Loy, Kaiming He, and Xiaoou Tang. Learning a deep convolutional network for image super-resolution. In *European conference on computer vision (ECCV)*, pages 184–199. Springer, 2014. [1](#)
- [11] Chao Dong, Chen Change Loy, Kaiming He, and Xiaoou Tang. Image super-resolution using deep convolutional networks. *IEEE transactions on pattern analysis and machine intelligence (PAMI)*, 38(2):295–307, 2015. [2](#)
- [12] Chao Dong, Chen Change Loy, and Xiaoou Tang. Accelerating the super-resolution convolutional neural network. In *European conference on computer vision (ECCV)*, pages 391–407. Springer, 2016. [3](#)
- [13] Alexey Dosovitskiy, Lucas Beyer, Alexander Kolesnikov, Dirk Weissenborn, Xiaohua Zhai, Thomas Unterthiner, Mostafa Dehghani, Matthias Minderer, Georg Heigold, Sylvain Gelly, et al. An image is worth 16x16 words: Transformers for image recognition at scale. *arXiv preprint arXiv:2010.11929*, 2020. [3](#)
- [14] Jinjin Gu and Chao Dong. Interpreting super-resolution networks with local attribution maps. In *Computer Vision and Pattern Recognition (CVPR)*, pages 9199–9208. IEEE/CVF, 2021. [11](#), [13](#)
- [15] Yong Guo, Jian Chen, Jingdong Wang, Qi Chen, Jie Zhang Cao, Zeshuai Deng, Yanwu Xu, and Mingkui Tan. Closed-loop matters: Dual regression networks for single image super-resolution. In *Computer Vision and Pattern Recognition (CVPR)*, pages 5407–5416. IEEE/CVF, 2020. [3](#)
- [16] Gao Huang, Yulin Wang, Kangchen Lv, Haojun Jiang, Wenhui Huang, Pengfei Qi, and Shiji Song. Glance and focus networks for dynamic visual recognition. *IEEE Transactions on Pattern Analysis and Machine Intelligence (PAMI)*, 45(4):4605–4621, 2022. [3](#)
- [17] Jia-Bin Huang, Abhishek Singh, and Narendra Ahuja. Single image super-resolution from transformed self-exemplars. In *Computer Vision and Pattern Recognition (CVPR)*, pages 5197–5206. IEEE/CVF, 2015. [6](#)
- [18] Zheng Hui, Xiumei Wang, and Xinbo Gao. Fast and accurate single image super-resolution via information distillation network. In *Computer Vision and Pattern Recognition (CVPR)*, pages 723–731. IEEE/CVF, 2018. [3](#)
- [19] Jiwon Kim, Jung Kwon Lee, and Kyoung Mu Lee. Accurate image super-resolution using very deep convolutional networks. In *Computer Vision and Pattern Recognition (CVPR)*, pages 1646–1654. IEEE/CVF, 2016. [3](#)
- [20] Xiangtao Kong, Hengyuan Zhao, Yu Qiao, and Chao Dong. Classsr: A general framework to accelerate super-resolution networks by data characteristic. In *Computer Vision and Pattern Recognition (CVPR)*, pages 12016–12025. IEEE/CVF, 2021. [1](#)
- [21] Christian Ledig, Lucas Theis, Ferenc Huszár, Jose Caballero, Andrew Cunningham, Alejandro Acosta, Andrew Aitken, Alykhan Tejani, Johannes Totz, Zehan Wang, et al. Photo-realistic single image super-resolution using a generative adversarial network. In *Computer Vision and Pattern Recognition (CVPR)*, pages 4681–4690. IEEE/CVF, 2017. [3](#)
- [22] Bingchen Li, Xin Li, Yiting Lu, Sen Liu, Ruoyu Feng, and Zhibo Chen. Hst: Hierarchical swin transformer for compressed image super-resolution. In *European Conference on*

- Computer Vision (ECCV)*, pages 651–668. Springer, 2022. 1, 2
- [23] Kunchang Li, Yali Wang, Junhao Zhang, Peng Gao, Guanglu Song, Yu Liu, Hongsheng Li, and Yu Qiao. Uniformer: Unifying convolution and self-attention for visual recognition. *IEEE Transactions on Pattern Analysis and Machine Intelligence (PAMI)*, 2023. 3, 4
- [24] Wenbo Li, Xin Lu, Jiangbo Lu, Xiangyu Zhang, and Jiaya Jia. On efficient transformer and image pre-training for low-level vision. *arXiv preprint arXiv:2112.10175*, 3(7):8, 2021. 7, 8, 11, 13
- [25] Y Li, K Zhang, J Cao, R Timofte, and L LocalViT Van Gool. Bringing locality to vision transformers. *arXiv preprint arXiv:2104.05707*, 2021. 3
- [26] Jingyun Liang, Jiezhong Cao, Guolei Sun, Kai Zhang, Luc Van Gool, and Radu Timofte. Swinir: Image restoration using swin transformer. In *International Conference on Computer Vision (ICCV)*, pages 1833–1844. IEEE, 2021. 1, 2, 3, 5, 7, 8, 11, 13
- [27] Bee Lim, Sanghyun Son, Heewon Kim, Seungjun Nah, and Kyoung Mu Lee. Enhanced deep residual networks for single image super-resolution. In *Computer Vision and Pattern Recognition Workshops (CVPR-W)*, pages 136–144. IEEE/CVF, 2017. 2, 3, 6, 7, 8
- [28] Ze Liu, Yutong Lin, Yue Cao, Han Hu, Yixuan Wei, Zheng Zhang, Stephen Lin, and Baining Guo. Swin transformer: Hierarchical vision transformer using shifted windows. In *International Conference on Computer Vision (ICCV)*, pages 10012–10022. IEEE, 2021. 1, 2
- [29] Zhisheng Lu, Juncheng Li, Hong Liu, Chaoyan Huang, Linlin Zhang, and Tiejiong Zeng. Transformer for single image super-resolution. In *Computer Vision and Pattern Recognition (CVPR)*, pages 457–466. IEEE/CVF, 2022. 1, 3
- [30] Xiaotong Luo, Yuan Xie, Yulun Zhang, Yanyun Qu, Cuihua Li, and Yun Fu. Latticenet: Towards lightweight image super-resolution with lattice block. In *European conference on computer vision (ECCV)*, pages 272–289. Springer, 2020. 3
- [31] Ziwei Luo, Haibin Huang, Lei Yu, Youwei Li, Haoqiang Fan, and Shuaicheng Liu. Deep constrained least squares for blind image super-resolution. In *Proceedings of the IEEE/CVF Conference on Computer Vision and Pattern Recognition*, pages 17642–17652, 2022. 3
- [32] David Martin, Charless Fowlkes, Doron Tal, and Jitendra Malik. A database of human segmented natural images and its application to evaluating segmentation algorithms and measuring ecological statistics. In *International Conference on Computer Vision (ICCV)*, volume 2, pages 416–423. IEEE, 2001. 6
- [33] Yusuke Matsui, Kota Ito, Yuji Aramaki, Azuma Fujimoto, Toru Ogawa, Toshihiko Yamasaki, and Kiyoharu Aizawa. Sketch-based manga retrieval using manga109 dataset. *Multimedia Tools and Applications*, 76:21811–21838, 2017. 6
- [34] Lingchen Meng, Hengduo Li, Bor-Chun Chen, Shiyi Lan, Zuxuan Wu, Yu-Gang Jiang, and Ser-Nam Lim. Adavit: Adaptive vision transformers for efficient image recognition. In *Computer Vision and Pattern Recognition (CVPR)*, pages 12309–12318. IEEE/CVF, 2022. 3
- [35] Ben Niu, Weilei Wen, Wenqi Ren, Xiangde Zhang, Lianping Yang, Shuzhen Wang, Kaihao Zhang, Xiaochun Cao, and Haifeng Shen. Single image super-resolution via a holistic attention network. In *European conference on computer vision (ECCV)*, pages 191–207. Springer, 2020. 3, 7, 8
- [36] Yajun Qiu, Qiang Zhu, Shuyuan Zhu, and Bing Zeng. Dual circle contrastive learning-based blind image super-resolution. *IEEE Transactions on Circuits and Systems for Video Technology*, 2023. 3
- [37] R Timofte, S Gu, J Wu, and L NTIRE Van Gool. challenge on single image super-resolution: Methods and results. In *Computer Vision and Pattern Recognition (CVPR)*, pages 18–22. IEEE/CVF, 2018. 6
- [38] Ashish Vaswani, Noam Shazeer, Niki Parmar, Jakob Uszkoreit, Llion Jones, Aidan N Gomez, Łukasz Kaiser, and Illia Polosukhin. Attention is all you need. *Advances in Neural Information Processing Systems (NeurIPS)*, 30, 2017. 3
- [39] Haiping Wu, Bin Xiao, Noel Codella, Mengchen Liu, Xiyang Dai, Lu Yuan, and Lei Zhang. Cvt: Introducing convolutions to vision transformers. In *International Conference on Computer Vision (ICCV)*, pages 22–31. IEEE, 2021. 3, 4
- [40] Tete Xiao, Mannat Singh, Eric Mintun, Trevor Darrell, Piotr Dollár, and Ross Girshick. Early convolutions help transformers see better. *Advances in Neural Information Processing Systems (NeurIPS)*, 34:30392–30400, 2021. 3, 4
- [41] Jinsu Yoo, Taehoon Kim, Sihaeng Lee, Seung Hwan Kim, Honglak Lee, and Tae Hyun Kim. Enriched cnn-transformer feature aggregation networks for super-resolution. In *Winter Conference on Applications of Computer Vision (WACV)*, pages 4956–4965. IEEE/CVF, 2023. 2, 3, 7, 8, 11, 13
- [42] Lei Yu, Xinpeng Li, Youwei Li, Ting Jiang, Qi Wu, Haoqiang Fan, and Shuaicheng Liu. Dipnet: Efficiency distillation and iterative pruning for image super-resolution. In *Proceedings of the IEEE/CVF Conference on Computer Vision and Pattern Recognition*, pages 1692–1701, 2023. 3
- [43] Roman Zeyde, Michael Elad, and Matan Protter. On single image scale-up using sparse-representations. In *International Conference Curves and Surfaces*, pages 711–730. Springer, 2012. 6
- [44] Jiale Zhang, Yulun Zhang, Jinjin Gu, Yongbing Zhang, Linghe Kong, and Xin Yuan. Accurate image restoration with attention retractable transformer. *arXiv preprint arXiv:2210.01427*, 2022. 1, 2, 3, 5, 7, 8, 11
- [45] Yulun Zhang, Kunpeng Li, Kai Li, Lichen Wang, Bineng Zhong, and Yun Fu. Image super-resolution using very deep residual channel attention networks. In *European conference on computer vision (ECCV)*, pages 286–301. Springer, 2018. 1, 3
- [46] Yulun Zhang, Yapeng Tian, Yu Kong, Bineng Zhong, and Yun Fu. Residual dense network for image super-resolution. In *Computer Vision and Pattern Recognition (CVPR)*, pages 2472–2481. IEEE/CVF, 2018. 1, 3
- [47] Qiang Zhu, Pengfei Li, and Qianhui Li. Attention retractable frequency fusion transformer for image super resolution. In *Proceedings of the IEEE/CVF Conference on Computer Vision and Pattern Recognition*, pages 1756–1763, 2023. 3

7. Supplementary

In this supplementary material, we provide additional information about model analysis and experimental results of Composite Fusion Attention Transformer (CFAT). We discuss the performance of our architecture and its variants along with their complexity in Sec. 7.1. In Sec. 7.2, we present the extensive results of an ablation study related to CFAT. We also compare the proposed model with various transformer-based state-of-the-art architectures graphically and based on LAM score [14] in the Sec. 7.3.

7.1. Extensive Model Analysis

We examine how the performance of our model varies alongside changes in complexity under two different settings: (i) channel size variation and (ii) model size variation. All the performances are evaluated on the BSD100 dataset for a scale of $\times 4$. In the first setting, we evaluate the complexity and the performance by increasing the value of channel counts from $96 \rightarrow 144 \rightarrow 180 \rightarrow 192$ as shown in Tab. 7. We observe a significant rise in performances (both PSNR and SSIM) when we widen the channel counts from $96 \rightarrow 144 \rightarrow 180$. However, it comes with a computational burden in terms of parameter counts and Multiply-Add operations. After 180, we observe a saturation in performance, e.g., only a 0.01dB improvement in PSNR when the channel is increased from 180 to 192.

After the channel-centric evaluation of CFAT, we set the channel count to 180 in our final model and compared it with various state-of-the-art architectures of the same channel count, as shown in Fig. 6. CFAT achieves the best performance and also maintains an excellent trade-off between parameter count and number of multiply-add operations. The Multiply-Add operations in HAT [6] and ART [44] are too high with moderate parameter counts, whereas SwinIR [26], EDT [24], and ACT [41] show the opposite trends. We observe an identical performance exhibited by ACT, ART, and HAT with little variations whereas the outcomes from EDT and SwinIR are comparatively lesser.

Table 7. Analysis of CFAT based on channel counts.

Channels	Params (M)	Multi-Adds (G)	PSNR/SSIM
192	25.01	102.6	28.18dB/0.7524
180	22.07	90.59	28.17dB/0.7524
144	14.35	59.22	27.99dB/0.7504
96	6.74	28.18	27.78dB/0.7469

We consider Dense Window Attention Blocks (DWAB) and Sparse Window Attention Blocks (SWAB) to be the basic units of CFAT and termed Window Attention Blocks (WAB). We compose three architectures, CFAT-l (large),

Table 8. Analysis of CFAT based on model size.

Models	Params (M)	Multi-Adds (G)	PSNR/SSIM
CFAT-l	34.89	142.08	28.25dB/0.7531
CFAT	22.07	90.59	28.17dB/0.7524
CFAT-s	14.35	59.22	27.99dB/0.7504
CFAT-r	13.52	56.27	27.93dB/0.7498

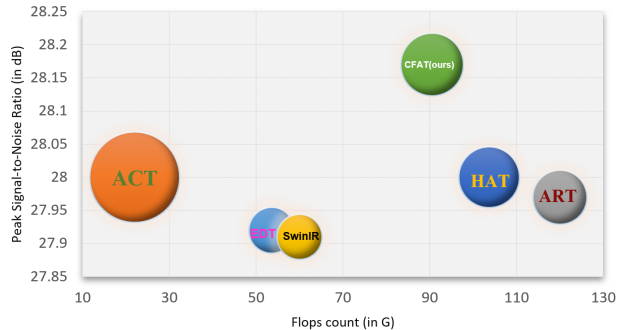


Figure 6. Performance vs Complexity plot of CFAT compare to other state-of-the-art models.

Performance: PSNR (on X-axis) in dB. **Complexity:** Flops (on Y-axis) in G and Parameters (area of the circle) in M

CFAT (medium), and CFAT-r (reduced), based on model depth, i.e., the number of WAB units present in CFAT. We take (8, 8, 8, 8, 8, 8, 8, 8) WAB units for CFAT-l, (8, 8, 8, 8, 8, 8, 8) for CFAT, and (8, 8, 8) for CFAT-r. Here, '8' signifies '4' pairs of Shifted-Dense Rectangular Window MSA ((SD)RW-MSA) and Shifted-Dense Triangular Window MSA ((SD)TW-MSA) arranged in an alternative fashion. We also consider another CFAT variant with 144 channels to compete with CFAT-r while finalizing our small variant. The corresponding parameters, Multiply-Add operations, and performances are displayed in Tab. 8. To finalize the small version, we prioritize more on performance over complexity. This table shows that CFAT with 144 channels yields higher performance than CFAT-r, while both possess identical complexity levels. Therefore, we designate CFAT with 144 channels as our small variant, CFAT-s.

7.2. Extensive Ablation Study

In this section, we investigate the performance variation of CFAT under the influence of different hyperparameters and model units. We evaluate all the model variants on the BSD100 dataset for scale factor $\times 4$ at distinct training iterations. We plot these outcomes in the X-axis along with their respective iterations in the Y-axis as displayed in Fig. 7. A large deviation in performance is observed when we evaluate the model within the first 17.5k iterations. Therefore, we adopt an averaging technique to keep the results steady at iterations of 5k, 7.5k, 10k, 12.5k, 15k, and 17.5k. The

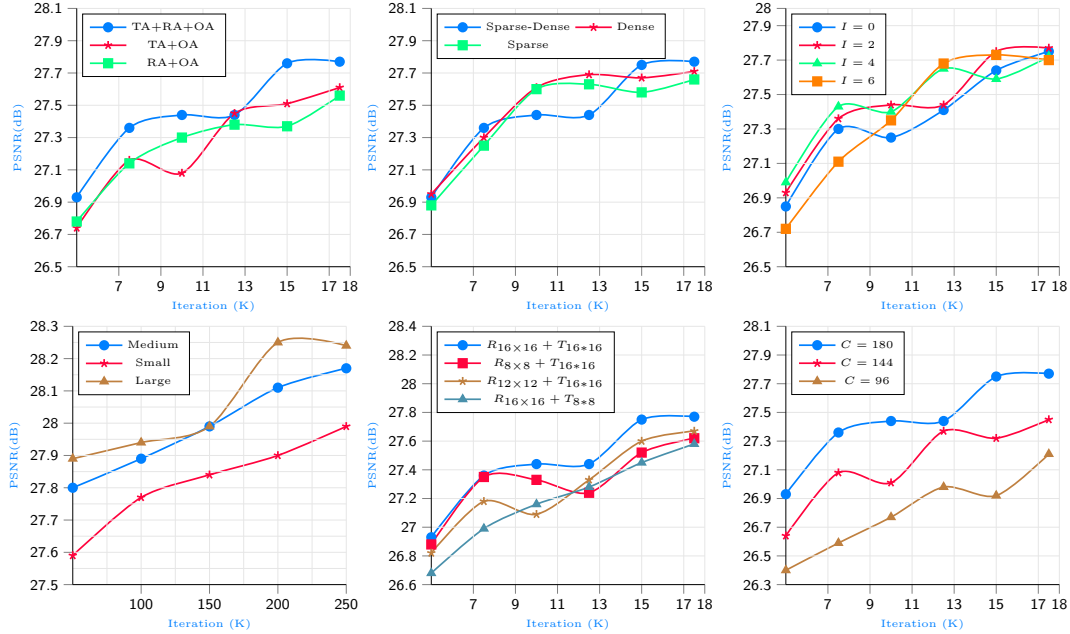


Figure 7. Iterative performance (PSNR in dB) comparison of the proposed CFAT for **Top-Left:** triangular vs rectangular vs overlapping attention, **Top-Middle:** sparse vs dense attention, **Top-Right:** various interval size, **Bottom-Left:** small vs medium vs large CFAT model, **Bottom-Middle:** various combinations of rectangular (8×8 , 12×12 , 16×16) with triangular (8×8 , 16×16) windows, and **Bottom-Right:** various channel lengths. [on BSD100($\times 4$) for epoch 70]

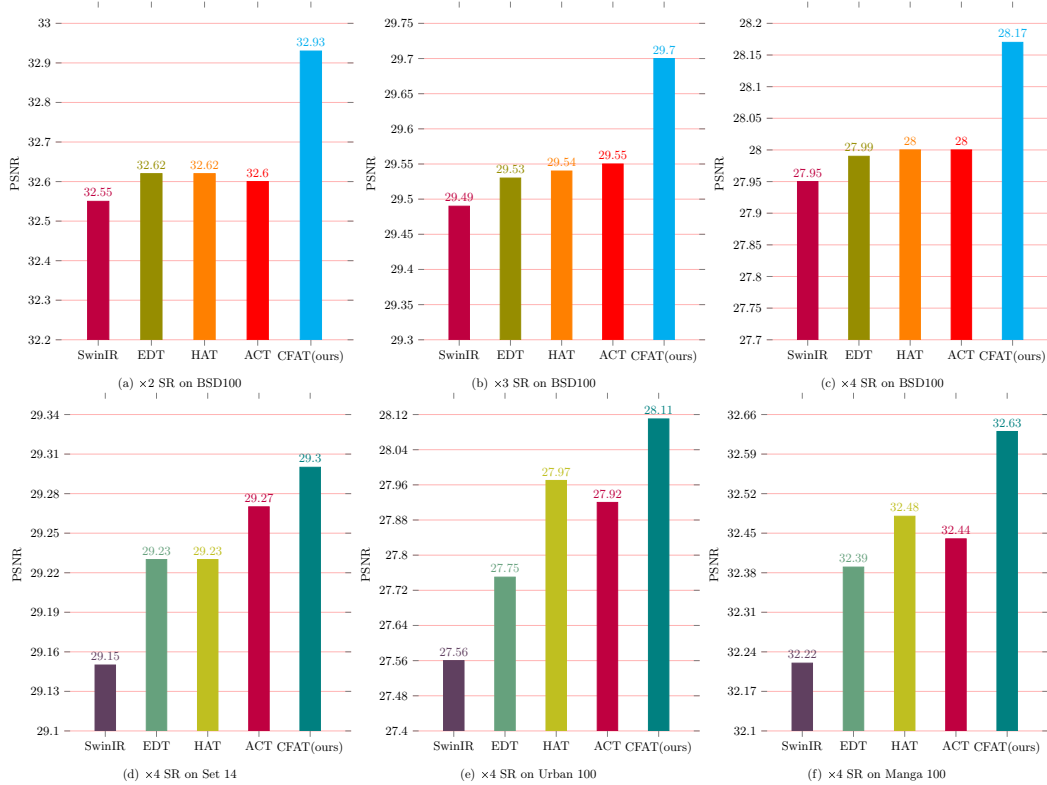


Figure 8. Comparing performance (PSNR in dB) of various state-of-the-art models with CFAT on **Top-Left:** BSD100 for scale 2, **Top-Middle:** BSD100 for scale 3, **Top-Right:** BSD100 for scale 4, **Bottom-Left:** Set14 for scale 4, **Bottom-Middle:** Urban100 for scale 4, and **Bottom-Right:** Manga109 for scale 4.

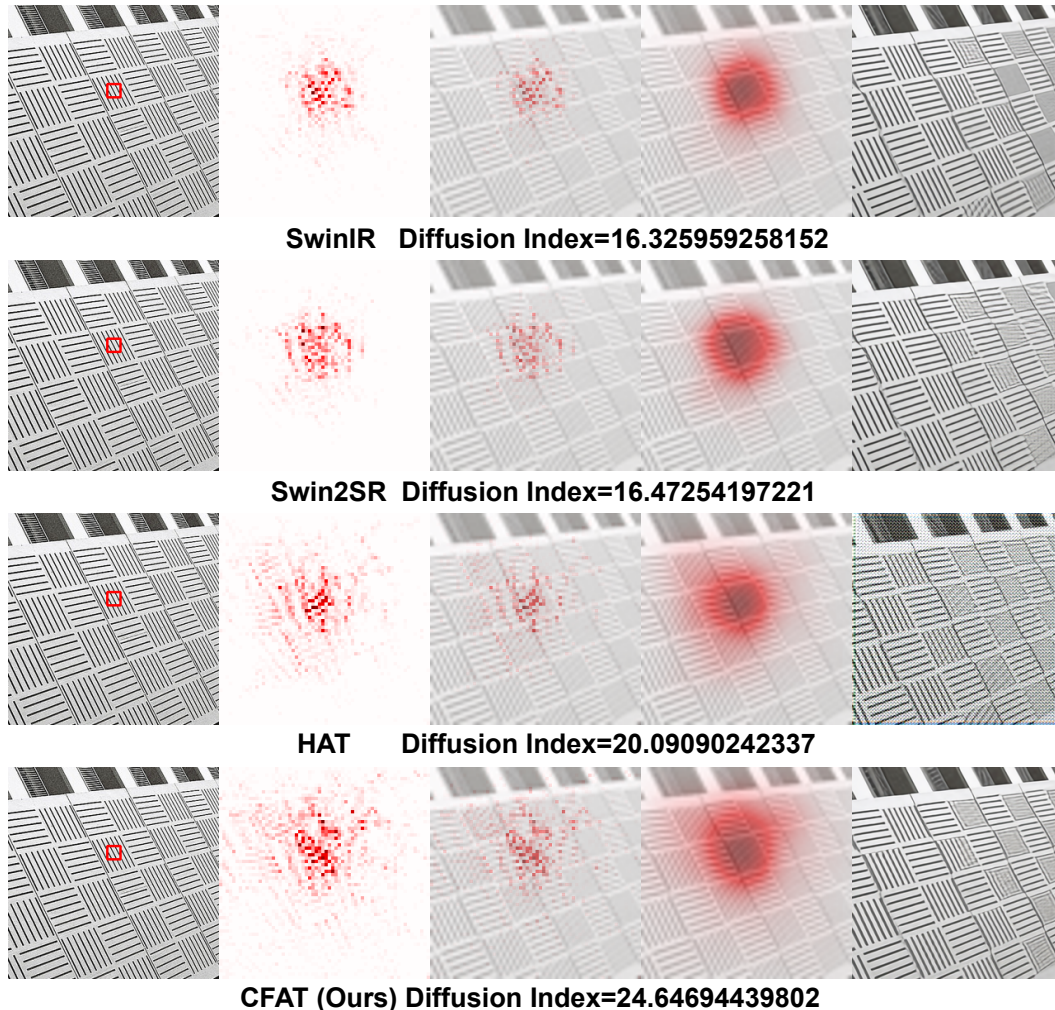


Figure 9. LAM results and corresponding Diffusion Index for CFAT and various SOTA methods.

averaging technique is implemented within the iteration or epoch range of $\pm 2.5k$ iteration or ± 5 epoch, respectively. The Top-Left plot shows the outcomes for models taking rectangular with overlapping attention, triangular with overlapping attention and rectangular, triangular with overlapping attention. We find that the last configuration yields the best results. The Top-Middle plot displays the significance of the combined dense-sparse attention-based model over isolated attention-based models. The Top-Right plot justifies selecting the interval size as '2' over others. The Bottom-Left plot maps out the performance of three CFAT-variants: CFAT-l, CFAT, and CFAT-s. Based on performances in the Bottom-Middle plot, we decide the best combination of window sizes for rectangular- and triangular-window attention. We map the model outcomes for three-channel counts (180, 144, and 96) in the Bottom-Right plot.

7.3. Extended Comparison with SOTA Architectures

In this section, we evaluate and compare the performance of the proposed architecture with other transformer-

based state-of-the-art models. The top three graphs (Top-Left, Top-Middle, and Top-Right) of Fig. 8 validate the supremacy of CFAT over SwinIR [26], EDT [24], ACT [41], and HAT [6] super-resolution (SR) architectures on BSD100 testing dataset for scales of $\times 2$, $\times 3$, and $\times 4$. These graphs also justify that our model possesses strong expressive power for every scale of super-resolution. As displayed in the bottom three graphs (Bottom-Left, Bottom-Middle, and Bottom-Right), we also verify the generalizability of CFAT by evaluating the performance on different testing datasets for a fixed scale ($\times 4$). All these performances are expressed in terms of peak-signal-to-noise ratio (PSNR). CFAT yields the highest PSNR values for all the above settings, as shown in this figure.

As visualized in Fig. 9, the LAM attributes [14] and Diffusion Index (DI) [14] of the proposed triangular window-based CFAT yield superior results than other rectangular window-based SOTA methods. To check the model's scalability in a low-data environment, all models are trained on the DIV2K dataset with batch size 16.